



# Exceptional visible-light photoelectrocatalytic activity of $\text{In}_2\text{O}_3/\text{In}_2\text{S}_3/\text{CdS}$ ternary stereoscopic porous heterostructure film for the degradation of persistent 4-fluoro-3-methylphenol



Yuting Xiao, Guohui Tian\*, Yajie Chen, Xin Zhang, Huiying Fu, Honggang Fu\*

Key Laboratory of Functional Inorganic Material Chemistry, Ministry of Education of the People's Republic of China, Heilongjiang University, Harbin 150080, PR China

## ARTICLE INFO

**Keywords:**  
 $\text{In}_2\text{O}_3/\text{In}_2\text{S}_3/\text{CdS}$   
 Stereoscopic porous heterostructure  
 Composite film  
 Photoelectrocatalysis

## ABSTRACT

In this work,  $\text{In}_2\text{O}_3/\text{In}_2\text{S}_3/\text{CdS}$  ternary stereoscopic porous heterostructure films were successfully fabricated via consecutive in situ ionic exchange reactions to degrade persistent 4-Fluoro-3-methylphenol through photoelectrocatalytic process. The optimized  $\text{In}_2\text{O}_3/\text{In}_2\text{S}_3/\text{CdS}$  ternary stereoscopic porous heterostructure film electrode showed much higher photoelectrocatalytic efficiency than the  $\text{In}_2\text{O}_3$  and  $\text{In}_2\text{O}_3/\text{In}_2\text{S}_3$  films. The resulting degradation reaction constant is about 3 and 2 times higher than that on  $\text{In}_2\text{O}_3$  and binary  $\text{In}_2\text{O}_3/\text{In}_2\text{S}_3$  films, respectively. The extraordinary higher degradation and mineralization efficiencies of the  $\text{In}_2\text{O}_3/\text{In}_2\text{S}_3/\text{CdS}$  composite film electrode come from the synergy of ternary components in the stereoscopic porous heterostructure. The existence of double type-II band alignment with nanosized interfaces in the ternary heterostructure can significantly improve charge transport and electron-hole separation. The stereoscopic porous architecture can greatly enhance visible light utilization and superhydrophilicity, and meanwhile facilitate the mass transport and accessibility of active sites. Ion chromatography, gas chromatography–mass spectrometry, total organic carbon analysis, active species trapping experiment as well as electron spin resonance techniques were employed to probe the degradation and the mineralization processes of 4-Fluoro-3-methylphenol. A unifying photoelectrocatalytic degradation route and mechanism is provided to explain the degradation and the mineralization processes. The generated more superoxide ions and holes promoted the defluorination process and favored the subsequent benzene ring cleavage and mineralization of low molecular weight fragments (e.g. carboxylic acids). This work provides a route to degrade persistent organic pollutants and realize efficient water contamination purification via efficient visible light photoelectrocatalytic process.

## 1. Introduction

In recent years, fluorine-containing phenolic compounds and their derivatives have been widely used in organic synthesis industry and in the production of disinfectants and pesticides [1,2]. These wastes can contain a wide range of chemical species and exist some years, so it is difficult to make efficient disposal [3]. Fluorine-containing phenolic derivatives are the priority pollutants according to United States Environmental Protection Agency (U.S. EPA) classification. Because they are widely applied and possess various toxicity effects, the release of these compounds is of environmental concern [4]. Among the derivatives, 4-Fluoro-3-methylphenol has received considerable attention to be used on the synthesis of a wide spectrum of chemical compound, and its release is of environmental concern [5]. Thus, it is necessary and meaningful to remove the toxic 4-Fluoro-3-methylphenol in water for protecting the security of drinking water. However, in recent years, 4-

Fluoro-3-methylphenol degradation has been seldom investigated.

During the past decades, photocatalytic technique was recognized as promising methods for the treatment of contaminated water solutions because of effective utilization of renewable solar power [6–12]. Meanwhile, electrochemical technology was also applied to the treatment of industrial wastewater and recalcitrant hazardous waste as an alternative to advanced oxidation processes due to its ease of operation and ability [13]. However, both of methods have themselves shortcomings. Most photocatalytic systems were operated in the suspensions, thus the recycling application of photocatalysts is restricted. As for electrochemical catalysis, reducing energy consumption is a development trend [14,15]. Recently, photoelectric-synergistic catalytic technology has shown great potential for the degradation of organic contaminants in comparison with individual photocatalysis and electrocatalysis [16,17]. In the photoelectrocatalytic process, there exists the synergistic effect between photocatalytic process and

\* Corresponding authors.

E-mail addresses: [tiangh@hlju.edu.cn](mailto:tiangh@hlju.edu.cn) (G. Tian), [fuhg@vip.sina.com](mailto:fuhg@vip.sina.com), [fuhg@hlju.edu.cn](mailto:fuhg@hlju.edu.cn) (H. Fu).

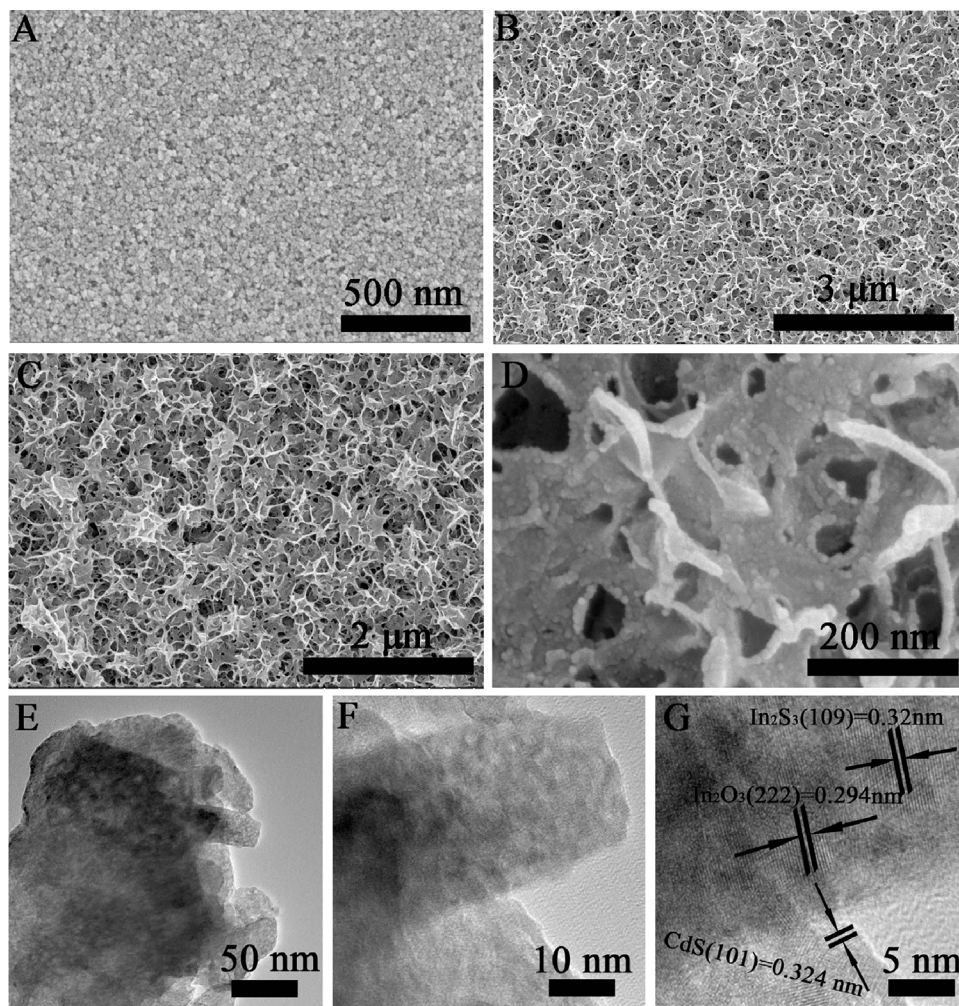


Fig. 1. SEM images of  $\text{In}_2\text{O}_3$  (A),  $\text{In}_2\text{O}_3/\text{In}_2\text{S}_3$  (B), and  $\text{In}_2\text{O}_3/\text{In}_2\text{S}_3/\text{CdS}$  (C, D). TEM (E, F) and HRTEM (G) images of the  $\text{In}_2\text{O}_3/\text{In}_2\text{S}_3/\text{CdS}$ .

electrochemical process. An applied bias potential can not only promote electrochemical degradation of target contaminants but also facilitate the photocatalysis by effectively separating charge pairs [18]. Meanwhile, the active species generated on the electrode surface via photocatalysis will decompose organic contaminants [19]. To this end, different strategies to enhance catalytic performance have been revealed in previous reports about photoelectrocatalytic studies.

In photoelectrocatalytic system, the perfect film photoelectrode should markedly promote separation and transportation of photo-generated charge, as well as improve the utilization efficiency of sunlight. Compared with single layer solid film, double-layer composite film can meet above requirements. For ideal photoelectrocatalytic double-layer composite films, the underlying film should possess high conductivity because of its critical role in connecting the upper film and outside circuit. The upper layer film acts as light absorber to convert solar energy into other kinds of energy. In the past studies, stereoscopic porous structures have proved to possess inspiring superiorities such as high light harvesting, abundant active sites, and sufficient transport of reactants and products. These excellent properties are greatly important in the enhancement of catalytic activity [20,21]. Therefore, inspired by these rewarding results, it is reasonable to fabricate heterostructure film constituting by the conductive substructure and stereoscopic porous superstructure to achieve satisfactory photoelectrocatalytic activity. However, within the scope of previous photoelectrocatalytic degradation reports, the relevant studies using proper stereoscopic porous heterostructure film as photoelectrode are deficient.

Considering the refractory degradation of fluorine-containing phenolic compounds, the objective of this study was to fabricate a high-

efficient  $\text{In}_2\text{O}_3/\text{In}_2\text{S}_3/\text{CdS}$  ternary stereoscopic porous heterostructure system with different roles for cooperative enhancement. In this work, the  $\text{In}_2\text{O}_3$  nanoparticles film with good electrical conductivity was first synthesized through a simple hydrothermal method, then it act as substrate and indium source to fabricate  $\text{In}_2\text{O}_3/\text{In}_2\text{S}_3$  binary stereoscopic porous film via an in situ anion exchange process. Further in situ cationic exchange cause the formation of  $\text{In}_2\text{O}_3/\text{In}_2\text{S}_3/\text{CdS}$  ternary stereoscopic porous heterostructure film with double type-II band alignment. So efficient charge carriers separation can be achieved. Moreover, the fabricated stereoscopic porous architecture can markedly improve visible light utilization and superhydrophilicity, and facilitate mass transport and accessibility of active sites compared to conventional flat solid films. These synergistic effects make the optimal  $\text{In}_2\text{O}_3/\text{In}_2\text{S}_3/\text{CdS}$  ternary stereoscopic porous heterostructure film exhibits exceptional photoelectrocatalytic degradation performance. Additionally, the photoelectrocatalytic degradation route and mechanism of 4-Fluoro-3-methylphenol over the fabricated ternary heterostructure film was also investigated with the help of gas chromatography tandem mass spectrometry and ion chromatography analysis techniques. Besides, the predominant role of different oxidants (photogenerated holes and  $\text{O}_2^{\cdot-}$ ) in contaminant transformation are also determined by the radical-trapping experiments.

## 2. Experimental section

### 2.1. Preparation of $\text{In}_2\text{O}_3$ nanoparticle film

The  $\text{In}_2\text{O}_3$  nanoparticle film was synthesized by hydrothermal

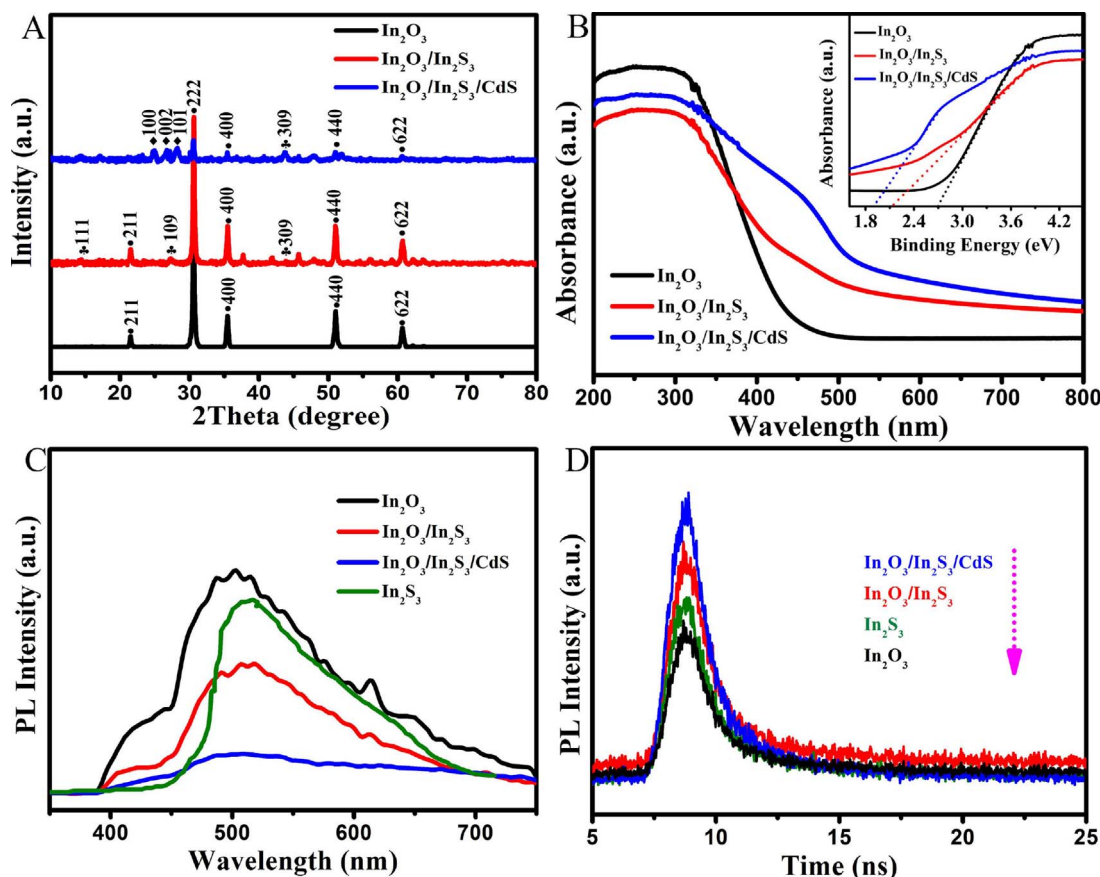


Fig. 2. XRD pattern (A), UV-vis diffuse reflectance spectra (B), steady-state PL (C) and time-resolved PL decay spectra (D) of the different samples.

reaction. In a typical case, 0.06 g  $\text{In}(\text{NO}_3)_3 \cdot 5\text{H}_2\text{O}$  was dissolved in 25 mL of distilled water under magnetic stirring. Then the clear solution was transferred into a 50 mL Teflon autoclave. After that, the cleaned FTO conductive glass (Asahi Glass, Japan) substrates ( $10 \times 60 \times 1 \text{ mm}^3$ ) were put in the Teflon reactor at a certain angle and autoclaved at 180 °C for 12 h. After reaction, the autoclave was cooled naturally. The as-obtained films were slightly rinsed with distilled water. Followed by a dry process at 50 °C and calcination at 350 °C for 2 h in air, the  $\text{In}_2\text{O}_3$  nanoparticle film was obtained.

#### 2.2. Fabrication of $\text{In}_2\text{O}_3/\text{In}_2\text{S}_3$ binary stereoscopic porous heterostructure films

Typical, 0.04 g L-Cysteine was added into the mixed solution containing 3 mL ethylene glycol and 22 mL ethanol, followed by stirring for 10 min. Then the mixed solution was transferred into a 50 mL Teflon reactor, and the FTO glasses containing the prepared  $\text{In}_2\text{O}_3$  nanoparticle films were also immersed in the solution at a certain angle. Thereafter, the Teflon autoclave was heated to 180 °C and maintained for 12 h. Subsequently, the autoclave was cooled to room temperature naturally. The obtained films were washed by ethanol and dried at 50 °C in air.

#### 2.3. Fabrication of the $\text{In}_2\text{O}_3/\text{In}_2\text{S}_3/\text{CdS}$ ternary stereoscopic porous heterostructure film

The ternary  $\text{In}_2\text{O}_3/\text{In}_2\text{S}_3/\text{CdS}$  stereoscopic heterojunction films were fabricated via a solvothermal growth reaction. Firstly, 0.02 g  $\text{CdCl}_2$  was dissolved in 25 mL ethanol. After magnetic stirring for 10 min, the mixture was transferred into a 50 mL Teflon reactor, and the FTO glasses containing the prepared  $\text{In}_2\text{O}_3/\text{In}_2\text{S}_3$  binary films were immersed in the solution at a certain angle. Then the mixed solutions were heated to 180 °C and maintained for different reaction time (10,

20, 30, and 40 min). Finally, the autoclave was cooled to room temperature naturally, the obtained films were washed by ethanol and dried at 50 °C in air.

#### 2.4. Characterization

The obtained products were characterized by X-ray diffraction (XRD, Bruker D8 Advance) with  $\text{Cu K}\alpha$  radiation ( $\lambda = 1.54178 \text{ \AA}$ ). The morphology of the obtained products was investigated by scanning electron microscopy (SEM, Hitachi S-4800, Japan) and transmission electron microscopy (TEM, JEOL 2100, Japan). The optical properties of the films were analyzed by UV-vis diffuse reflectance spectroscopy (UV-vis DRS) using a UV-vis spectrophotometer (Shimadzu UV-2550). The electronic states of the elements in the sample were analyzed using X-ray photoelectron spectroscopy (XPS, Kratos-AXIS ULTRA DLD, Al Ka X-ray source). Inductively coupled plasma optical emission spectroscopy (ICP-OES, Optima 7000DV, PerkinElmer) was used to measure material content. The scanning Kelvin probe (SKP) measurements (SKP5050 system, Scotland) were performed under normal laboratory conditions in an ambient atmosphere. A gold electrode was used as the reference electrode. Photoluminescence (PL) measurements were taken using a FL920 spectrophotometer (Edinburgh Instruments) with the photoexcitation wavelength set at 360 nm. Luminescence lifetimes were recorded on a single photon counting spectrometer using a microsecond pulse lamp as the excitation source (375 nm). The data were analyzed using software supplied by Edinburgh Instruments. The contact angle measurements of the films were conducted on an OCA20 goniometer from Dataphysics with an experimental error of  $\pm 1^\circ$  by the sessile drop method at room temperature using a water droplet with a volume of about 1  $\mu\text{L}$ . GC-MS analysis was carried out on an Agilent 6890GC/5973MSD with a DB-5 MS capillary column.

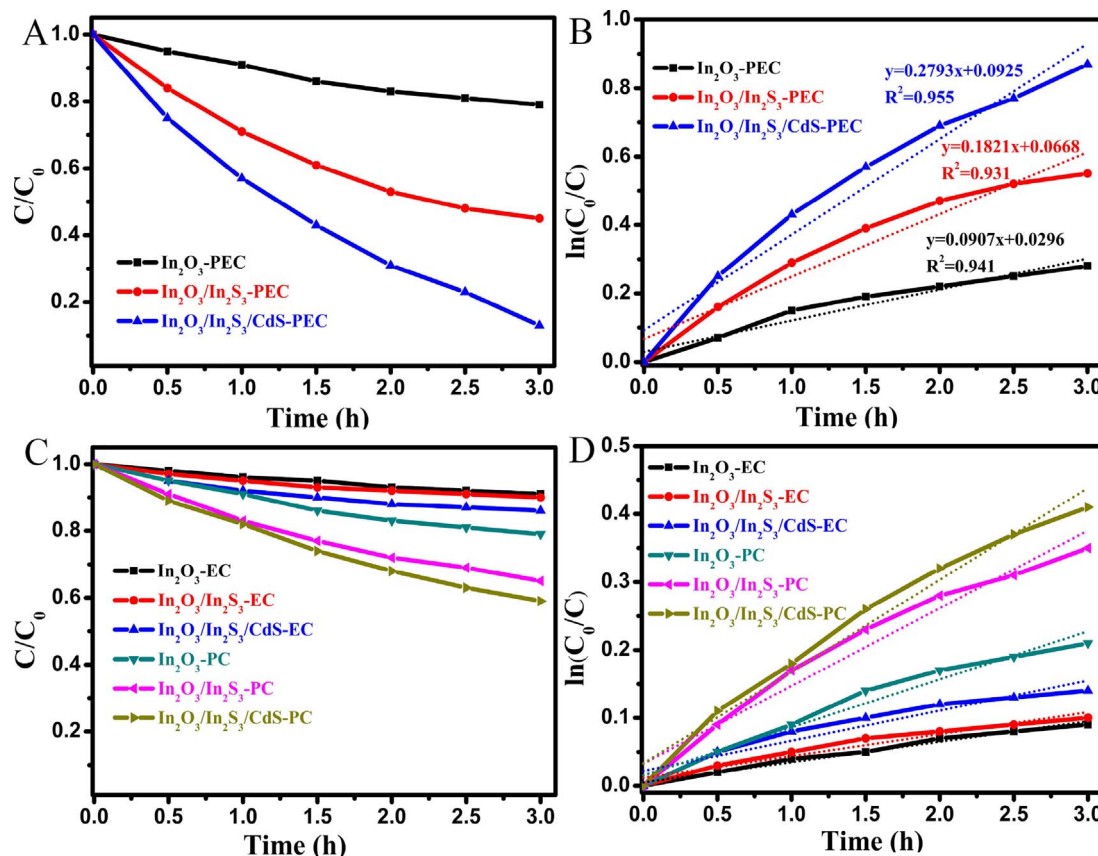


**Fig. 3.** (A) The degradation efficiency of 4-Fluoro-3-methylphenol over different samples during the PEC degradation process ( $\lambda > 420$  nm); (B) The corresponding kinetic analysis with the PEC degradation on different samples. (C) The comparison of the EC and PC degradation rate constant  $k$  over  $\text{In}_2\text{O}_3$ ,  $\text{In}_2\text{O}_3/\text{In}_2\text{S}_3$ , and  $\text{In}_2\text{O}_3/\text{In}_2\text{S}_3/\text{CdS}$  (visible light,  $\lambda > 420$  nm); (D) The kinetic analysis with the EC and PC degradation on the  $\text{In}_2\text{O}_3$ ,  $\text{In}_2\text{O}_3/\text{In}_2\text{S}_3$ ,  $\text{In}_2\text{O}_3/\text{In}_2\text{S}_3/\text{CdS}$ .

## 2.5. Photoelectrochemical test

Photoelectrochemical measurements of the obtained products were recorded by a BAS100B electrochemical analyzer (Bioanalytical Systems Inc., USA) in a standard three-compartment cell consisting of a working electrode, a Pt slice as the counter electrode, and saturated Ag/AgCl as the reference electrode. The working electrode was different samples. All photoelectrochemical experiments are carried out at ambient temperature (25 °C) in a 0.1 M solution (pH = 6.95). All photoelectrochemical experiments were carried out under visible light irradiation with a power density of 100 mW/cm<sup>2</sup>.

## 2.6. Photoelectrocatalytic degradation tests

The photoelectrochemical activities of the samples were evaluated by degradation of 4-Fluoro-3-methylphenol in an aqueous solution under visible light irradiation. Typical photoelectrochemical degradation process is arranged in this way: vigorous stirring of a 4-Fluoro-3-methylphenol solution (100 mL) with an initial concentration of 50 mg L<sup>-1</sup> and using 0.1 M  $\text{Na}_2\text{SO}_4$  as the electrolyte) was performed for 30 min in the dark to establish an adsorption–desorption equilibrium among the catalyst, contaminant and water. The working electrode was irradiated with visible light obtained from a 300W Xe lamp with bandpass filter of UV-cut 420 nm. The photoelectrocatalytic performances of the catalysts were immediately gauged by measuring the intensity changes of the optical absorption peaks by a UV-vis spectrophotometer (Shimadzu UV-2550). In the photoelectrochemical process, a series of reactive species, such as  $\text{h}^+$ ,  $\cdot\text{OH}$ , or  $\cdot\text{O}_2^-$ , are supposed to be involved. To detect the active species generated in the photoelectrochemical system, various scavengers, including isopropanol (IPA, 10 mmol L<sup>-1</sup>),  $\text{KBrO}_3$  (6 mmol L<sup>-1</sup>), ammonium oxalate (AO

(6 mmol L<sup>-1</sup>) and benzoquinone (BQ) (6 mmol L<sup>-1</sup>) were introduced into the solution. The method was similar to the above mentioned degradation of 4-Fluoro-3-methylphenol test.

The total organic carbon (TOC) analyzer (multi N/C 3000) was employed for mineralization degree analysis of the organic pollutants solutions. Prior to injection into the TOC analyzer, the samples were filtrated with a 0.45 μm Millipore filter. All experiments were carried out at least in duplicate. The reported values were within the experimental error range of (3%). GC-MS analysis was carried out on an Agilent 6890GC/5973MSD with a DB-5 MS capillary column. 5, 5-Dimethyl-1-pyrroline N-oxide (DMPO) spin trapping electron spin resonance (ESR) spectra were recorded with a Bruker A300 spectrometer at room temperature. General instrument settings are as follows: microwave power, 6.35 mW; modulation amplitude, 3 G; receiver gain,  $1 \times 10^3$ ; time constant, 10.24 ms; sweep time, 42 s; center field, 3507 G; sweep width, 80 G.

## 3. Results and discussion

The morphology and structure of the prepared films were characterized by scanning electron microscopy (SEM) and transmission electron microscopy (TEM). It can be clearly seen that the  $\text{In}_2\text{O}_3$  thin film is composed of dense nanoparticles (Fig. 1A). But the surface of the  $\text{In}_2\text{O}_3/\text{In}_2\text{S}_3$  binary composite film is covered by  $\text{In}_2\text{S}_3$  hierarchical porous framework structure, and the surface of  $\text{In}_2\text{S}_3$  nanosheets is smooth (Fig. 1B). For the  $\text{In}_2\text{O}_3/\text{In}_2\text{S}_3/\text{CdS}$  ternary heterostructure film, the integral hierarchical porous framework was maintained (Fig. 1C). But from the enlarged SEM image in Fig. 1D, uniformly-distributed nanoparticles can be observed on the surface of  $\text{In}_2\text{S}_3$  nanosheets. The existence and homogeneous distribution of Cd, In, S and O elements on the  $\text{In}_2\text{O}_3/\text{In}_2\text{S}_3/\text{CdS}$  ternary stereoscopic porous framework film can be

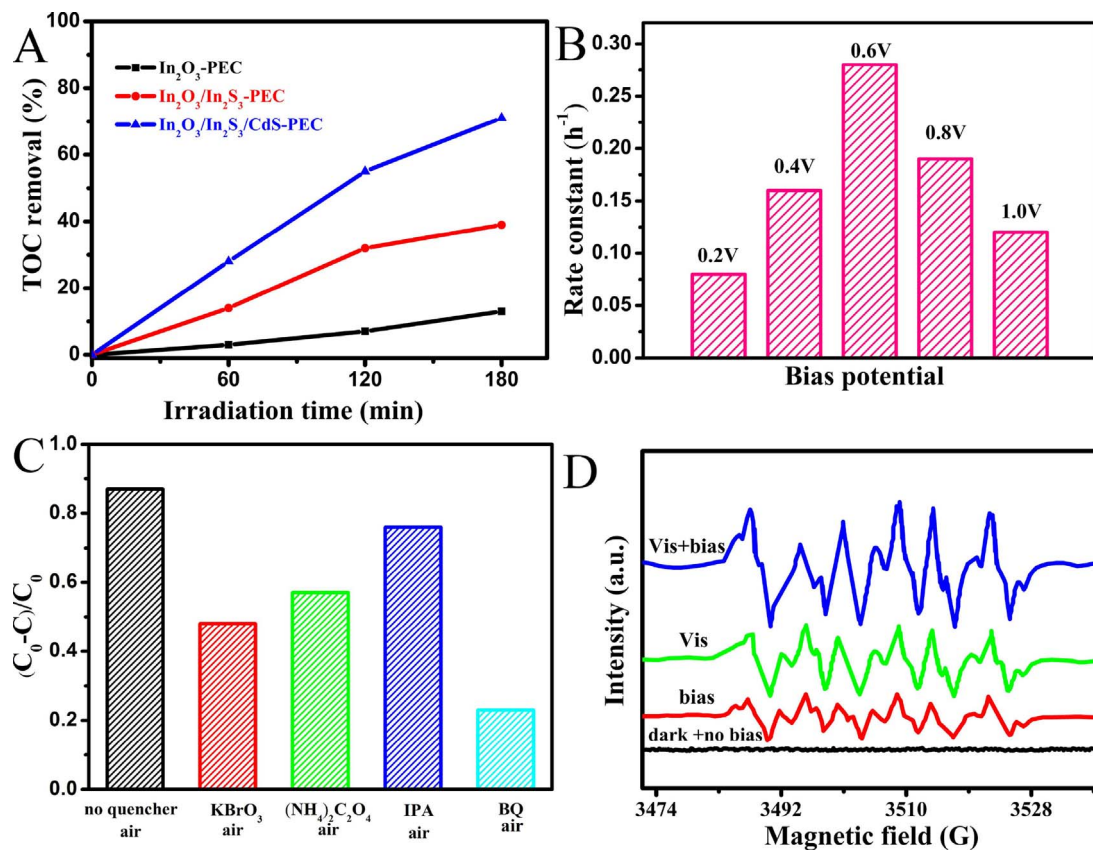


**Fig. 4.** (A) Total Organic Carbon (TOC) removal of the different samples during PEC degradation process. (B) The comparison of the PEC degradation activities of the  $\text{In}_2\text{O}_3/\text{In}_2\text{S}_3/\text{CdS}$  under different bias voltages. (C) Activities of the  $\text{In}_2\text{O}_3/\text{In}_2\text{S}_3/\text{CdS}$  with different scavengers during the PEC degradation under visible light irradiation. (D) The DMPO spin-trapping ESR spectra on  $\text{In}_2\text{O}_3/\text{In}_2\text{S}_3/\text{CdS}$  in methanol dispersion for the DMPO- $\text{O}_2^{\cdot-}$  radical adducts after different degradation processes of 4-Fluoro-3-methylphenol.

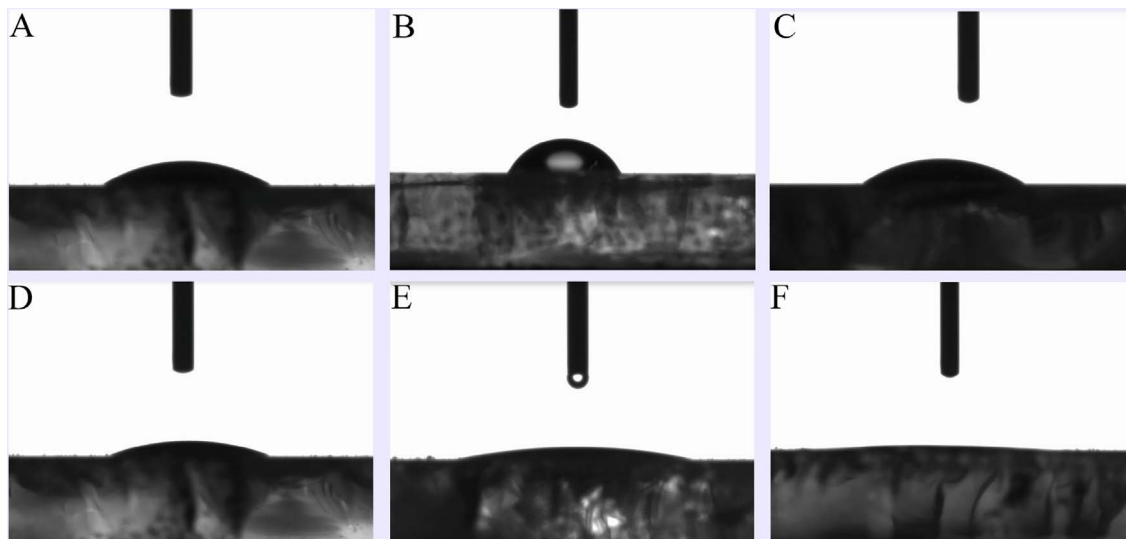


**Fig. 5.** (A), (B), and (C) are water contact angle photographs of  $\text{In}_2\text{O}_3$ ,  $\text{In}_2\text{O}_3/\text{In}_2\text{S}_3$ , and  $\text{In}_2\text{O}_3/\text{In}_2\text{S}_3/\text{CdS}$  under dark condition, respectively. (D), (E), and (F) are water contact angle photographs of the corresponding samples after 2 h visible light irradiation.

further observed from the elemental mapping analysis (Fig. S1-3). The cross-sectional SEM image (Fig. S4) suggests the thickness of the  $\text{In}_2\text{O}_3/\text{In}_2\text{S}_3/\text{CdS}$  film is around hundreds of nanometers. The nanosheet structure of the  $\text{In}_2\text{O}_3/\text{In}_2\text{S}_3/\text{CdS}$  ternary composite was also observed in TEM image (Fig. 1E, F). The HRTEM image in Fig. 1G shows that the lattice planes of 0.294, 0.32, and 0.324 nm are consistent with the (222), (109), and (101) planes of the  $\text{In}_2\text{O}_3$ ,  $\text{In}_2\text{S}_3$ , and  $\text{CdS}$ , respectively [22–24]. These neighboring surfaces constituted heterostructure

interfaces, which can benefit better charge separation and transfer. The Scheme S1 shows that fabrication process of the  $\text{In}_2\text{O}_3/\text{In}_2\text{S}_3/\text{CdS}$  ternary stereoscopic porous heterostructure film includes hydrothermal growth process and subsequent two consecutive in situ ionic exchange reactions. Moreover, the amounts of  $\text{In}_2\text{S}_3$  nanosheets were time-dependent, which can be seen from Fig. S5. When the reaction time is 3 h, sparse  $\text{In}_2\text{S}_3$  can be found (Fig. S5 A). With the increase of reaction time (6, 12 h), the formed  $\text{In}_2\text{S}_3$  film became more dense and uniform (Fig.

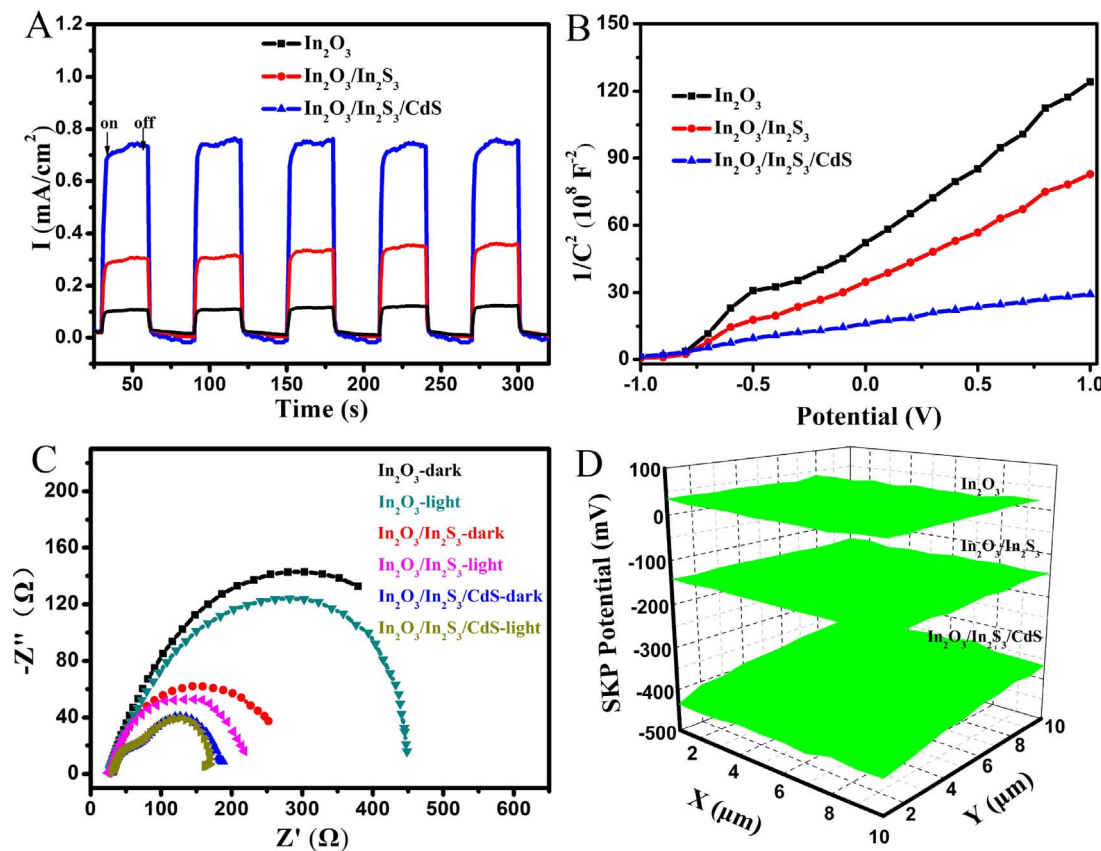


Fig. 6. The chronoamperometry (A), Mott-Schottky plots (B), EIS Nyquist plots (C), and work function maps (D) of the different samples.

S5B), and stereoscopic porous structure can be clearly seen (Fig. S5C). Similarly, the amounts of CdS nanoparticles were also increased with the increase of cationic exchange reaction time (Fig. S6).

The XRD patterns of  $\text{In}_2\text{O}_3$ ,  $\text{In}_2\text{O}_3/\text{In}_2\text{S}_3$ , and  $\text{In}_2\text{O}_3/\text{In}_2\text{S}_3/\text{CdS}$  composite are shown in Fig. 2A. In the XRD pattern of  $\text{In}_2\text{O}_3/\text{In}_2\text{S}_3$ , apart from the diffraction peaks indexed to cubic  $\text{In}_2\text{O}_3$  (JCPDC No.71-2194) [25], the other diffraction planes of (109), (440), and (309) matched with tetragonal  $\text{In}_2\text{S}_3$  [26]. For the XRD pattern of the  $\text{In}_2\text{O}_3/\text{In}_2\text{S}_3/\text{CdS}$  composite, besides the diffraction peaks of  $\text{In}_2\text{O}_3$  and  $\text{In}_2\text{S}_3$ , the diffraction peaks located at 26.5°, 43.9°, and 52.1° are attributed to the (111), (220), and (311) facet crystal planes of cubic CdS [27]. The UV-vis absorption spectra in Fig. 2B showed that, compared with the absorption edge of the  $\text{In}_2\text{O}_3$  film, there have a red-shift of the spectrum and increased visible light absorption for the binary  $\text{In}_2\text{O}_3/\text{In}_2\text{S}_3$  and ternary  $\text{In}_2\text{O}_3/\text{In}_2\text{S}_3/\text{CdS}$  due to the introduction of narrow band gap  $\text{In}_2\text{S}_3$  and CdS. This enhanced visible light absorption has a positive effect on the photoelectrocatalytic activity. The XPS spectra in Fig. S7 and S8 illustrate the presence of the In, O, S, and Cd elements in the  $\text{In}_2\text{O}_3/\text{In}_2\text{S}_3/\text{CdS}$ . As shown in Fig. S8b, the phenomena of spin orbit separation (7.5 eV) between XPS peaks of In 3d5/2 (444.5 eV) and In 3d3/2 (452.0 eV) suggest the existence of  $\text{S}^{2-}$  [28,29]. However, compared with the In 3d peaks of  $\text{In}_2\text{O}_3$ , there has slight red shift for the In 3d peaks of  $\text{In}_2\text{O}_3/\text{In}_2\text{S}_3$  and  $\text{In}_2\text{O}_3/\text{In}_2\text{S}_3/\text{CdS}$  (Fig. S9), which can be attributed to the interaction between the semiconductors due to the formation of heterojunction.

In order to elucidate the charge carrier kinetics and investigate charge separation transfer at the interfaces of the heterostructure composites, steady-state and time-resolved PL tests were performed. As shown in Fig. 2C, compared with  $\text{In}_2\text{O}_3$ ,  $\text{In}_2\text{S}_3$  and  $\text{In}_2\text{O}_3/\text{In}_2\text{S}_3$ , the addition of CdS causes the obvious PL quenching, further suggesting a lower electron-hole recombination rate for the  $\text{In}_2\text{O}_3/\text{In}_2\text{S}_3/\text{CdS}$ . The time-resolved PL spectra results are presented in Fig. 2D and Table S1. Obviously, the  $\text{In}_2\text{O}_3/\text{In}_2\text{S}_3/\text{CdS}$  shows the longest lifetime

( $\tau_1 = 3.12$  ns). Charge carriers with longer lifetime represent more opportunities for participation in the catalytic reactions, thus contributing to the enhancement of catalytic activity [30].

The  $\text{In}_2\text{O}_3/\text{In}_2\text{S}_3/\text{CdS}$  shows the increased surface area ( $89.6 \text{ m}^2 \text{ g}^{-1}$ ) than the  $\text{In}_2\text{O}_3/\text{In}_2\text{S}_3$  ( $57.5 \text{ m}^2 \text{ g}^{-1}$ ) and  $\text{In}_2\text{O}_3$  ( $28.9 \text{ m}^2 \text{ g}^{-1}$ ) according to the result of  $\text{N}_2$ -sorption-desorption isotherms (Fig. S10). Meanwhile, the typical H3 hysteresis loop and a relatively wide pore size distribution indicate the formation of the slit-shaped mesopores due to the aggregates of composite nanosheets in the porous network structure. The large surface area and porous network structure of the  $\text{In}_2\text{O}_3/\text{In}_2\text{S}_3/\text{CdS}$  ternary composite could provide more exposed active sites for photoelectrocatalytic reaction.

The photoelectrocatalytic (PEC) performance of the different samples were conducted under visible-light ( $\lambda > 420$  nm). From Fig. S11 we can see that the blank process and photolysis almost played no role in the degradation of 4-Fluoro-3-methylphenol. Fig. 3A displays PEC degradation processes of 4-Fluoro-3-methylphenol with different catalysts. Clearly, the  $\text{In}_2\text{O}_3/\text{In}_2\text{S}_3/\text{CdS}$  photoelectrode showed the highest PEC activity, and 87.3% of 4-Fluoro-3-methylphenol could be degraded after 180 min (Fig. S12). The experimental data in Fig. 3B were found to fit approximately a pseudo-first-order kinetic model ( $\ln (\text{Co}/\text{C}_t) = kt$ ), and their corresponding kinetics constants are listed in Table S2. Apparently, the kinetic constant  $k$  ( $0.279 \text{ h}^{-1}$ ) of the  $\text{In}_2\text{O}_3/\text{In}_2\text{S}_3/\text{CdS}$  photoelectrode is about two and three times faster than that of  $\text{In}_2\text{O}_3/\text{In}_2\text{S}_3$  ( $0.182 \text{ h}^{-1}$ ) and  $\text{In}_2\text{O}_3$  ( $0.091 \text{ h}^{-1}$ ) photoelectrodes, respectively. The highest degradation efficiency of the  $\text{In}_2\text{O}_3/\text{In}_2\text{S}_3/\text{CdS}$  photoelectrode arises from the synergistic effect of the different components among the  $\text{In}_2\text{O}_3/\text{In}_2\text{S}_3/\text{CdS}$  composite. The corresponding total organic carbon (TOC) results also demonstrated that the optimized  $\text{In}_2\text{O}_3/\text{In}_2\text{S}_3/\text{CdS}$  photoelectrode exhibited the highest activity toward organic pollutants mineralization, and 71% of the initial TOC was removed from the solution after 180 min (Fig. 4A). Moreover, the TOC mineralization efficiencies of the different photoelectrodes were lower

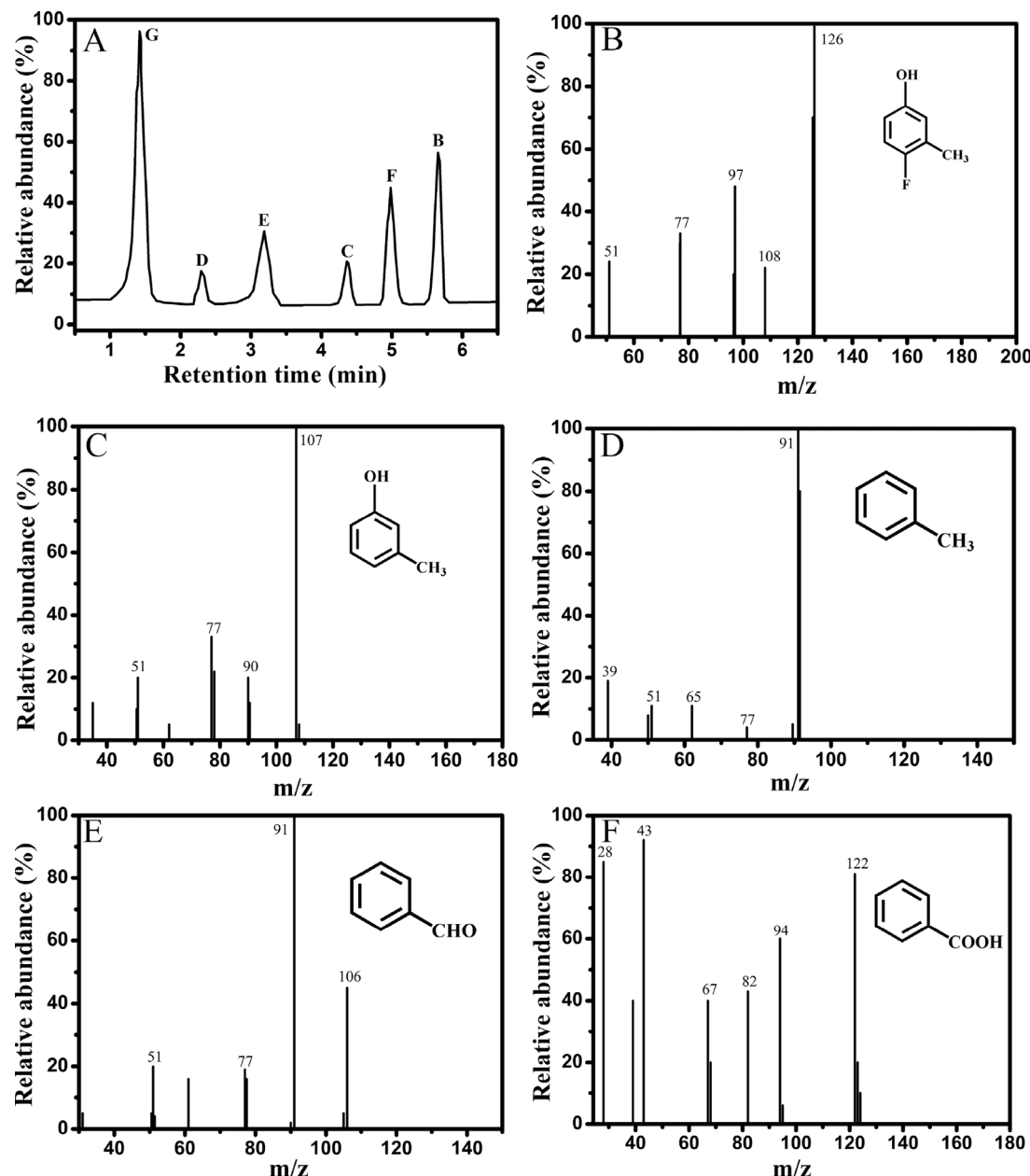


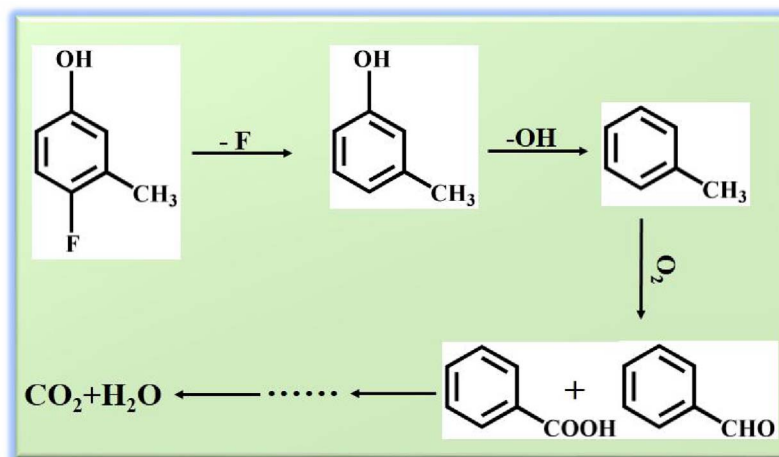
**Fig. 7.** Total gas chromatogram (A) and mass spectra of peaks (B), (C), (D), (E), and (F) obtained from photoelectrocatalytic degradation of 4-Fluoro-3-methylphenol over  $\text{In}_2\text{O}_3/\text{In}_2\text{S}_3/\text{CdS}$  photoelectrode after 3 h visible light irradiation (extracted by dichloromethane).

than the corresponding degradation efficiencies (Table S2). So a prolonged PEC time would need for complete mineralization. Similar trends were also found in PC and EC processes, the optimal  $\text{In}_2\text{O}_3/\text{In}_2\text{S}_3/\text{CdS}$  photoelectrode also showed higher degradation ability than  $\text{In}_2\text{O}_3$  and  $\text{In}_2\text{O}_3/\text{In}_2\text{S}_3$  electrodes under both PC and EC processes (Fig. 3C, D). 41.9% and 14.7% of 4-Fluoro-3-methylphenol were removed by PC and EC processes after 180 min, respectively. The sum (56.6%) of PC and EC processes is lower than that (87.3%) of the PEC process. Similar results can also be observed for the  $\text{In}_2\text{O}_3$  and  $\text{In}_2\text{O}_3/\text{In}_2\text{S}_3$  electrodes (Table S2), further manifesting that there should have a significant synergy between PC and EC processes.

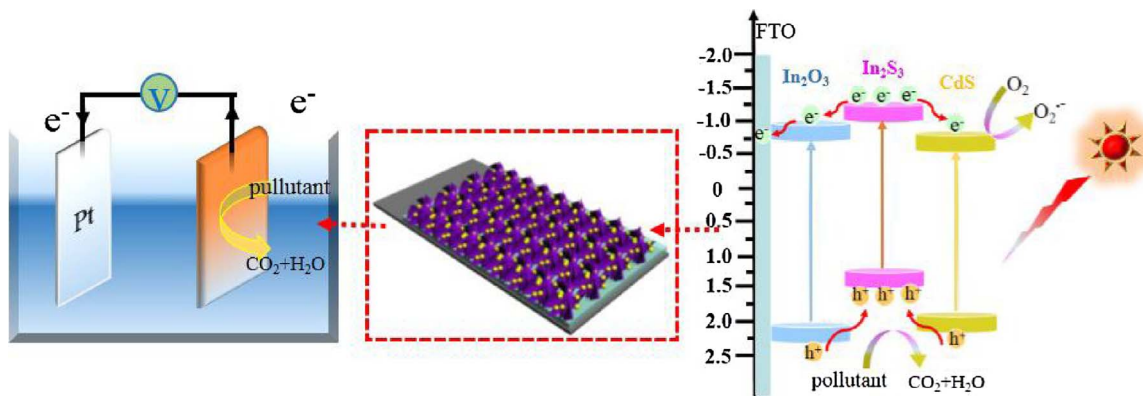
Meanwhile, defluorination efficiencies of the 4-Fluoro-3-methylphenol in various processes were also investigated by ion chromatography. As shown in Fig. S13A, the defluorination efficiencies of the three paths gradually increased with the extension of degradation time, and the defluorination efficiency of PEC process is much higher than that of PC and EC process. Moreover, the  $\text{In}_2\text{O}_3/\text{In}_2\text{S}_3/\text{CdS}$

photoelectrode shows higher defluorination efficiency than  $\text{In}_2\text{O}_3/\text{In}_2\text{S}_3$  and  $\text{In}_2\text{O}_3$  photoelectrodes in PEC process (Fig. S13B).

On the other hand, the factors (e.g. CdS content and bias voltage) affecting PEC activity were investigated. When the content of CdS is suitable, the optimal PEC removal efficiency can be obtained (Fig. S14). Moreover, the influence of bias voltage is very remarkable (Fig. 4B). As the bias voltage increases, the PEC activity of the  $\text{In}_2\text{O}_3/\text{In}_2\text{S}_3/\text{CdS}$  photoelectrode first increased and then decreased. The degradation rate of 4-Fluoro-3-methylphenol reached the maximum when the bias voltage was 0.6 V. The suitable external potential could effectively promote the photogenerated electrons transfer to the counter electrode through external circuit, inhibiting the recombination of photogenerated charges. When the bias potential is too high, the degradation rate of the 4-Fluoro-3-methylphenol decreased because of the decreased number of photogenerated carriers caused by the reallocation of space charge layer. Surface morphology and structure also have remarkable influence on degradation performance. As shown in Fig. S16, the PEC



**Scheme 1.** Schematic reaction pathway for photoelectrocatalytic degradation of 4-Fluoro-3-methylphenol over  $\text{In}_2\text{O}_3/\text{In}_2\text{S}_3/\text{CdS}$  ternary stereoscopic porous heterostructure film photoelectrode.



**Scheme 2.** The schematic illustration for the photoelectrocatalytic mechanism of organic pollutants over the  $\text{In}_2\text{O}_3/\text{In}_2\text{S}_3/\text{CdS}$  photoelectrode.

performance of the  $\text{In}_2\text{O}_3/\text{In}_2\text{S}_3$  film with stereoscopic porous framework is higher than that of  $\text{In}_2\text{O}_3/\text{In}_2\text{S}_3$  film with densification surface structure (Fig. S15). Remarkably, the stereoscopic porous structure can provide more active sites and improve quick transport of medium molecules and visible light utilization.

To get insight into the PEC mechanism of the  $\text{In}_2\text{O}_3/\text{In}_2\text{S}_3/\text{CdS}$  photoelectrode and clarify the contribution of different active species to the PEC degradation of 4-Fluoro-3-methylphenol, the active species trapping experiments were conducted. As shown in Fig. 4C, the PEC degradation rates of 4-Fluoro-3-methylphenol were not apparently retarded by the addition of IPA (trapping species of  $\cdot\text{OH}$ ) (Fig. 4C), which indicates the secondary role of  $\cdot\text{OH}$  in PEC degradation process. On the contrary, the PEC degradation of 4-Fluoro-3-methylphenol is dramatically inhibited after the addition of BQ, AO, and  $\text{KBrO}_3$ , which are the trapping species of  $\cdot\text{O}_2^-$ , hole, and electrons, respectively. On the basis of above results, it can be concluded that  $\cdot\text{O}_2^-$ , hole ( $\text{h}^+$ ) and photo-generated electrons play important role in the degradation of 4-Fluoro-3-methylphenol. The holes can directly oxidize organic pollutants. Photogenerated electrons could be trapped by the absorbed  $\text{O}_2$  to form  $\cdot\text{O}_2^-$  to degrade 4-Fluoro-3-methylphenol. The formation of  $\cdot\text{O}_2^-$  was further proved by DMPO spin-trapping electron-spin resonance (ESR) techniques. As shown in Fig. 4D, clear six-fold ESR peak with characteristics of DMPO- $\cdot\text{O}_2^-$  signals appeared during electrolysis at  $-0.6\text{ V vs Ag/AgCl}$  after visible light irradiation [31,32]. Moreover, the DMPO- $\cdot\text{O}_2^-$  signal intensity under bias voltage and visible light irradiation is higher than that under single bias voltage or visible light irradiation. But no ESR signal was observed in the absence of visible light radiation and applied bias. It is apparent that the produced DMPO- $\cdot\text{O}_2^-$  species are attributed to the reduction of  $\text{O}_2$  by negatively biased  $\text{In}_2\text{O}_3/\text{In}_2\text{S}_3/\text{CdS}$  photoelectrode under visible light irradiation.

Because the photoelectrocatalytic reactions happen on the electrode/electrolyte interface, so the hydrophilic property of film plays a considerable role in influencing the photoelectrocatalytic oxidation ability [33]. As shown in Fig. 5A–C, the obtained three kinds of films all show hydrophilic properties with relatively small water contact angles. After visible light irradiation, the water droplet spreads quickly as soon as it contacts the surface of the films (Fig. 5D–F). Especially, the contact angle of the ternary  $\text{In}_2\text{O}_3/\text{In}_2\text{S}_3/\text{CdS}$  film decreases to almost  $0^\circ$ , which is smaller than that of the  $\text{In}_2\text{O}_3$  and  $\text{In}_2\text{O}_3/\text{In}_2\text{S}_3$  films. Such excellent superhydrophilicity of the ternary  $\text{In}_2\text{O}_3/\text{In}_2\text{S}_3/\text{CdS}$  film can be ascribed to the high surface roughness and large capillary force of the stereoscopic porous heterostructure (Fig. 5) [33,34]. The superhydrophilicity (a water contact angle of less than  $5^\circ$ ) of the  $\text{In}_2\text{O}_3/\text{In}_2\text{S}_3/\text{CdS}$  stereoscopic porous heterostructure film contributes to the adsorption of water soluble pollutants and further PEC degradation.

To elucidate the effect of photoelectron generation and electron–hole recombination rate on the photoelectrocatalytic activity, the photoelectronic response of different films to visible light was investigated. As shown in Fig. 6A, the  $\text{In}_2\text{O}_3/\text{In}_2\text{S}_3/\text{CdS}$  photoelectrode showed the strongest photocurrent response. Such enhanced photocurrent density can be ascribed to the more electrons generated by the increased light absorption and the quick charge separation. Mott–Schottky tests were also performed to interpret the mechanism for electrical conduction properties. The  $\text{In}_2\text{O}_3/\text{In}_2\text{S}_3/\text{CdS}$  electrode showed the smallest slope, it indicates the highest electron density, favoring the PEC reactions (Fig. 6B). Electrochemical impedances spectroscopy (EIS) measurements were applied to evaluate the charge transfer property. As shown in Fig. 6C and Fig. S17, among the three samples, the arc radius of the  $\text{In}_2\text{O}_3/\text{In}_2\text{S}_3/\text{CdS}$  electrode is always the smallest one under visible light illumination and in the dark, suggesting

its lowest resistance for interfacial charge transfer. Moreover, it is apparent that the sizes of the arc radii are obviously reduced under visible light irradiation. Once the photoelectrodes were irradiated by visible light, the excessive photogenerated electrons will flow to external circuit via FTO electrode, so reducing the interface resistance.

The Scanning Kelvin Probe (SKP) is an extremely sensitive instrument that can measure the direction of interface electric fields and study the electronic properties [35,36]. The lowest work function of the  $\text{In}_2\text{O}_3/\text{In}_2\text{S}_3/\text{CdS}$  film implies that the additional photoelectron transfer from the surface layer to the inner conducting stratum, and then transfer to the external circuit (Fig. 6D). Thus, the opportunity of electron-hole recombination was dramatically reduced, and favoring to increase PEC activity.

The photoelectrocatalytic degradation pathway and process of 4-Fluoro-3-methylphenol in the  $\text{In}_2\text{O}_3/\text{In}_2\text{S}_3/\text{CdS}$  photoelectrocatalytic system were investigated through the major intermediate products detection by GC-MS. Fig. S18 and Fig. 7 show the intermediate products of different degradation time, and the concentrations of the degradation products of 4-Fluoro-3-methylphenol after different time visible light irradiation (extracted by dichloromethane) were also shown in Table S3. Fig. 7 shows the gas chromatogram and corresponding mass spectra of peaks B, C, D, E and F of 4-Fluoro-3-methylphenol PEC degradation product obtained from 3 h visible light irradiation. According to the GC-MS analysis (Fig. 7), the peak B with retention time of 5.7 min ( $m/z = 126$ ) is attributed to the initial 4-Fluoro-3-methylphenol, and the other peaks appearing at 2.27 (peak D,  $m/z = 91$ ), 3.21 (peak E,  $m/z = 106$ ), 4.34 (peak C,  $m/z = 107$ ), and 4.97 (peak F,  $m/z = 122$ ) min were found to methylbenzene, benzaldehyde, 3-methylphenol, benzoic acid, respectively. Based on the GC-MS analysis results, a possible pathway of 4-Fluoro-3-methylphenol degradation is put forward in Scheme 1. First, 4-Fluoro-3-methylphenol is defluorinated to form 3-methylphenol. The generation of  $\text{F}^-$  species in solution during PEC process manifests that the substantial degradation of 4-Fluoro-3-methylphenol and the resulting organic intermediates have occurred. After defluorination, the produced 3-methylphenol is dehydroxylated to form methylbenzene. Subsequently, methylbenzene is oxidized by active radicals to form benzaldehyde and Benzoic acid. The following ring cleavage leads to the formation of the aliphatic carboxylic acids and other short chain carboxylic acids containing several carbonyl bonds ( $\text{C}=\text{O}$ ) and alkenyl bonds ( $\text{C}=\text{C}$ ), despite these intermediates were not detected by GC-MS, which is similar to the other reports [37,38]. These intermediates are finally degraded into  $\text{CO}_2$  and  $\text{H}_2\text{O}$ . Our study demonstrates that the photoelectrocatalytic condition can lead to defluorination, carbonylation, and ring cleavage of aromatic compounds. These test results also suggested that the aromatic ring cleavage is the rate-limiting step toward eventual mineralization.

As discussed above, there are three consecutive steps in this photoelectrocatalytic degradation process: light harvesting, charge separation and migration to the photocatalyst surface, and the following surface adsorption and redox reaction. In the  $\text{In}_2\text{O}_3/\text{In}_2\text{S}_3/\text{CdS}$  ternary stereoscopic porous heterostructure film system, under visible-light illumination, the photoexcited electrons in the conduction band of  $\text{In}_2\text{S}_3$  can be transferred to  $\text{In}_2\text{O}_3$  and  $\text{CdS}$  because of the fact that the conduction band of  $\text{In}_2\text{S}_3$  is higher than that of  $\text{In}_2\text{O}_3$  and  $\text{CdS}$  (Scheme 2). The double-transfer route can greatly improve the separation efficiency of electron-hole pairs. The conduction bands of  $\text{In}_2\text{O}_3$ ,  $\text{In}_2\text{S}_3$ , and  $\text{CdS}$  are negative than that of  $E_0$  ( $\text{O}_2/\cdot\text{O}_2^-$ ) (-0.046 eV vs NHE), the electrons in the conduction band can reduce  $\text{O}_2$  to  $\cdot\text{O}_2^-$ , which is consistent with the experimental result. Under external bias voltage, the electrons in the  $\text{In}_2\text{O}_3$  transfer to the FTO electrode and reach the surface of cathode electrode (Pt slice) through an external circuit. At the same time, the holes in the valence band of  $\text{In}_2\text{O}_3$  and  $\text{CdS}$  transferred to the valence band of  $\text{In}_2\text{S}_3$  and degrade the pollutant directly. The enhanced photogenerated electron-hole separation in the  $\text{In}_2\text{O}_3/\text{In}_2\text{S}_3/\text{CdS}$  system was revealed by photoelectrochemical and SKP tests (Fig. 6).

Moreover, the  $\text{In}_2\text{O}_3/\text{In}_2\text{S}_3/\text{CdS}$  film electrode showed relatively high recycling stability (Fig. S19 and 20). The integral stereoscopic porous structure is well kept, which can be seen from the SEM image of the  $\text{In}_2\text{O}_3/\text{In}_2\text{S}_3/\text{CdS}$  film after photoelectrocatalytic degradation. The ICP-OES test result shows that almost no metal ions can be detected in the solution after photoelectrocatalytic degradation. The  $\text{In}_2\text{O}_3/\text{In}_2\text{S}_3/\text{CdS}$  ternary stereoscopic heterostructure presents double type-II modes and can quickly separate the charge carriers, which makes the  $\text{In}_2\text{O}_3/\text{In}_2\text{S}_3/\text{CdS}$  ternary stereoscopic porous structure film photoelectrode avoid obvious changes in structure and composition.

## 4. Conclusions

In this work, effective degradation of persistent 4-Fluoro-3-methylphenol was executed through the photoelectric-synergistic catalytic technology using the  $\text{In}_2\text{O}_3/\text{In}_2\text{S}_3/\text{CdS}$  ternary stereoscopic porous architecture film system. The stereoscopic porous channel structure is fit for quick diffusion of reactants, improved separation of photogenerated charge, enhanced visible-light absorption and superhydrophilicity. In this photoelectrocatalytic system, active radicals (e.g. photogenerated holes and  $\text{O}_2^-$ ) play predominant role in the conversion and mineralization of organic contaminants. Thus, the investigation of the photoelectrocatalytic degradation route and mechanism for 4-Fluoro-3-methylphenol in this study can provide new insights into the intrinsic relationship between different redox-actives and photoelectrocatalysis, and also offer a new strategy to improve the organic pollutants degradation ability and expand photoelectrochemical application.

## Acknowledgments

This research was supported by the National Natural Science Foundation of China (21631004, 51772079, 21376065, 51672073), the Natural Science Foundation of Heilongjiang Province of China (B2017009), Application Technology Research and Development Projects in Harbin (2013AE4BW051), and Special Fund of Technological Innovation Talents in Harbin City (No. 2015RAQXJ003).

## Appendix A. Supplementary data

Supplementary data associated with this article can be found, in the online version, at <https://doi.org/10.1016/j.apcatb.2017.12.015>.

## References

- [1] M.B. McConville, T.D. Hubert, C.K. Remucal, Environ. Sci. Technol. 50 (2016) 9998–10006.
- [2] C.K. Remucal, Environ. Sci. Process Impacts 16 (2014) 628–653.
- [3] J.H. Carey, M.E. Fox, J. Great Lakes Res. 7 (1981) 234–241.
- [4] H. Hori, A. Yamamoto, K. Koike, S. Kutsuna, M. Murayama, A. Yoshimoto, R. Arakawa, Appl. Catal. B Environ. 82 (2008) 58–66.
- [5] J.H. Jeon, J.Y. Yang, N. Chung, H.S. Lee, J. Agric. Food. Chem. 60 (2012) 12349–12354.
- [6] Y. Liu, X. Liu, Y. Zhao, D.D. Dionysiou, Appl. Catal. B Environ. 213 (2017) 74–86.
- [7] C. Tang, L.F. Liu, Y.L. Li, Z.F. Bian, Appl. Catal. B Environ. 201 (2017) 41–47.
- [8] Y.L. Li, Y.Y. Bian, H.X. Qin, Y.X. Zhang, Z.F. Bian, Appl. Catal. B Environ. 206 (2017) 293–299.
- [9] Z.F. Bian, J. Zhua, H.X. Li, J. Photochem. Photobio. C: Photochem. Rev. 28 (2016) 72–86.
- [10] Z.F. Bian, F.L. Cao, J. Zhu, H.X. Li, Environ. Sci. Technol. 49 (2015) 2418–2424.
- [11] F.F. Chen, F.L. Cao, H.X. Li, Z.F. Bian, Langmuir 31 (2015) 3494–3499.
- [12] H.X. Q, Y.Y. Bian, Y.X. Zhang, L.F. Liu, Z.F. Bian, Chin. J. Chem. 35 (2017) 203–208.
- [13] P.T. Almazán-Sánchez, S. Cotillas, C. Sáez, M.J. Solache-Ríos, V. Martínez-Miranda, P. Cañizares, I. Linares-Hernández, M.A. Rodrigo, Appl. Catal. B Environ. 213 (2017) 190–197.
- [14] H. Sun, G. Li, X. Nie, H. Shi, P.K. Wong, H. Zhao, T. An, Environ. Sci. Technol. 48 (2014) 9412–9419.
- [15] L. Hu, C.C. Fong, X. Zhang, L.L. Chan, P.K. Lam, P.K. Chu, K.Y. Wong, M. Yang, Environ. Sci. Technol. 50 (2016) 4430–4438.
- [16] M. Seol, J.W. Jang, S. Cho, J.S. Lee, K. Yong, Chem. Mater. 25 (2013) 184–189.
- [17] J. Tang, Y. Zhang, B. Kong, Y. Wang, P. Da, J. Li, A.A. Elzatahry, D. Zhao, X. Gong, G. Zheng, Nano Lett. 14 (2014) 2702–2708.

[18] Y. Sun, C. Liu, D.C. Grauer, J. Yano, J.R. Long, P. Yang, C.J. Chang, *J. Am. Chem. Soc.* 135 (2013) 17699–17702.

[19] J.T. Kirner, J.J. Stracke, B.A. Gregg, R.G. Finke, *ACS Appl. Mater. Inter.* 6 (2014) 13367–13377.

[20] S. Sun, W. Wang, L. Zhang, *J. Phys. Chem. C* 116 (2012) 19413–19418.

[21] Y.J. Alireza Kargar, S.J. Kim, C.T. Riley, X.Q. Pan, D. Wang, *ACS Nano* 7 (2013) 11112–11120.

[22] Y.X. Pan, Y. You, S. Xin, Y. Li, G. Fu, Z. Cui, Y.L. Men, F.F. Cao, S.H. Yu, J.B. Goodenough, *J. Am. Chem. Soc.* 11 (2017) 4123–4129.

[23] W. Qiu, M. Xu, X. Yang, F. Chen, Y. Nan, J. Zhang, H. Iwai, H. Chen, *J. Mater. Chem.* 21 (2011) 13327–13333.

[24] Z. Jiang, K. Qian, C. Zhu, H. Sun, W. Wan, J. Xie, H. Li, P.K. Wong, S. Yuan, *Appl. Catal. B Environ.* 210 (2017) 194–204.

[25] X. Wang, J. Su, H. Chen, G.D. Li, Z. Shi, H. Zou, X. Zou, *ACS Appl. Mater. Inter.* 9 (2017) 16335–16342.

[26] Y. Li, G. Chen, Q. Wang, X. Wang, A. Zhou, Z. Shen, *Adv. Funct. Mater.* 20 (2010) 3390–3398.

[27] Z. Xu, H. Li, Z. Wu, J. Sun, Z. Ying, J. Wu, N. Xu, *J. Mater. Chem. C* 4 (2016) 7501–7507.

[28] J. Zhou, G. Tian, Y. Chen, Y. Shi, C. Tian, K. Pan, H. Fu, *Sci. Rep.* 4 (2014) 4027.

[29] J. Li, Y. Ma, Z. Ye, M. Zhou, H. Wang, C. Ma, D. Wang, P. Huo, Y. Yan, *Appl. Catal. B Environ.* 204 (2017) 224–238.

[30] X. Jiao, Z. Chen, X. Li, Y. Sun, S. Gao, W. Yan, C. Wang, Q. Zhang, Y. Lin, Y. Luo, Y. Xie, *J. Am. Chem. Soc.* 139 (2017) 7586–7594.

[31] S. Zavahir, Q. Xiao, S. Sarina, J. Zhao, S. Bottle, M. Wellard, J. Jia, L. Jing, Y. Huang, J.P. Blinco, H. Wu, H.-Y. Zhu, *ACS Catal.* 6 (2016) 3580–3588.

[32] S. Xia, X. Zhang, X. Zhou, Y. Meng, J. Xue, Z. Ni, *Appl. Catal. B Environ.* 214 (2017) 78–88.

[33] D. Zang, H. Yi, Z. Gu, L. Chen, D. Han, X. Guo, S. Wang, M. Liu, L. Jiang, *Adv. Mater.* 29 (2017).

[34] H. Liu, Y. Chen, G. Tian, Z. Ren, C. Tian, H. Fu, *Langmuir* 31 (2015) 5962–5969.

[35] H. Yan, C. Tian, L. Wang, A. Wu, M. Meng, L. Zhao, H. Fu, *Angew. Chem. Int. Ed.* 54 (2015) 6325–6329.

[36] L. Wang, G. Tian, Y. Chen, Y. Xiao, H. Fu, *Nanoscale* 8 (2016) 9366–9375.

[37] S. Lan, J. Feng, Y. Xiong, S. Tian, S. Liu, L. Kong, *Environ. Sci. Technol.* 51 (2017) 6560–6569.

[38] M. Pan, H. Zhang, G. Gao, L. Liu, W. Chen, *Environ. Sci. Technol.* 49 (2015) 6240–6248.